

Ultrabroadband low-crosstalk dense lithium niobate waveguides by Floquet engineering

Zhiyuan Lin, Wange Song^{✉,*}, Jiacheng Sun, Xueyun Li, Chunyu Huang, Shengjie Wu, Haoran Xin, Shining Zhu, and Tao Li^{✉†}

National Laboratory of Solid State Microstructures, Key Laboratory of Intelligent Optical Sensing and Manipulations, Jiangsu Key Laboratory of Artificial Functional Materials, School of Physics, College of Engineering and Applied Sciences, Nanjing University, Nanjing, 210093, China



(Received 13 July 2023; revised 18 September 2023; accepted 19 October 2023; published 2 November 2023)

Integrated photonic chips have gradually become a significant option for information transmission and processing, in which the integration density will play an increasingly important role similar to that witnessed in integrated circuits. To date, great efforts have been made for silicon-on-insulator wafers to achieve dense integration with low crosstalk, although it remains quite challenging in the emerging lithium-niobate-on-insulator (LNOI) platform. Here, we report a strategy utilizing *Floquet-mode-index modulation* to realize broadband zero crosstalk with minimal impact on other performance metrics on the LNOI chips. The underlying physics of zero crosstalk is attributed to the collapse of the *Floquet quasienergy*, which is further experimentally verified by ultrabroadband low-crosstalk transmissions with low excess loss. Moreover, we demonstrate broadband eight-channel light transmissions in a compact LNOI waveguide array, showing an advantage over the conventional ones in comparison. Our work provides an alternative approach for improving the integration density of on-chip photonic circuits, opening up different possibilities for dense waveguide applications in the promising LNOI platform.

DOI: 10.1103/PhysRevApplied.20.054005

I. INTRODUCTION

Integrated photonics is becoming increasingly significant in information processing technology, including chip-scale optical interconnects [1,2], space-division multiplexing [3,4], parallel computing [5–7], and sensing [8]. The increasing complexity and versatility of a photonic integrated chip require more and more components, thus miniaturization with low power consumption in photonic devices is highly desired. However, the waveguide mode exhibits exponentially decaying evanescent fields in the cladding, which would overlap to give rise to near-field coupling. Although this near-field coupling can be harnessed to achieve directional coupler or splitter functions, they also result in significant interchannel crosstalk, thus limiting the chip's integration density and scalability [9–14]. To overcome the long-standing challenge of crosstalk reduction in high-density photonic chips, great efforts have been made by incorporating superlattices [9,10,15], extreme-skin-depth waveguides [13,14,16], artificial-gauge-bending designs [17–20], etc. These approaches mainly focused on a silicon-on-insulator (SOI) wafer that has a large refractive-index contrast and high fabrication accuracy, which provides high flexibility in designing tiny

subwavelength metamaterials or bending the waveguides without encountering high scattering losses. Moreover, achieving broadband low crosstalk is still quite challenging.

Lithium niobate on insulator (LNOI), as a promising photonic integration platform, has received much consideration in recent years due to its advantages, such as high-speed electro-optical modulators and nonlinear-signal generation [21–27]. Yet, low refractive-index contrast and relatively immature fabrication techniques of the LNOI make it difficult to directly transplant existing schemes into the LNOI platform. Recently, it was revealed that, instead of bending the waveguide, periodically modulating on-site potentials also exhibited high flexibility for manipulating optical fields, giving rise to nontrivial Floquet topological phases known as *bimorphic Floquet topological insulators* [28]. This can circumvent additional losses entailed by curved waveguide trajectories in conventional Floquet topological insulators [29–31], and inspires us to utilize waveguide-mode-index modulation to reduce crosstalk without introducing excessive bending losses on the LNOI chips.

Here, we propose an alternative approach to realize broadband zero crosstalk by Floquet engineering of the mode index in LNOI waveguides. By periodically varying the waveguides along the light-propagation direction, the resulting Floquet-quasienergy spectrum will collapse

* songwange@nju.edu.cn

† taoli@nju.edu.cn

under certain driving conditions, giving rise to the inhibition of light-tunneling effects. As such, an effective zero coupling can be obtained to achieve low-crosstalk light transmission, which is further verified in LNOI experiments with ultrabroadband and robust performances. In addition, eight-channel low-crosstalk broadband light transmissions are demonstrated, suggesting practical applications in massive photonic integrations. This work provides an alternative method for achieving high-density waveguides with broadband low crosstalk, which are promising for advancing device performance on the LNOI platform.

II. FLOQUET ANALYSIS OF BROADBAND ZERO COUPLING

We start our analysis on an on-site Floquet modulation with frequency $\Omega = 2\pi/p$ that is applied to a one-dimensional waveguide array along the light-propagation direction, z , with driving phase difference φ between adjacent waveguides. In the paraxial approximation, such a tight-binding lattice can be described by

$$H(z) = \sum_{n=1}^N \beta_0 a_n^\dagger a_n + \sum_{n=1}^N A \sin \left(\Omega z + \theta + (-1)^n \frac{\varphi}{2} \right) a_n^\dagger a_n + \sum_{n=1}^{N-1} \kappa_{n,n+1} a_n^\dagger a_{n+1} + h.c., \quad (1)$$

and light evolution is governed by a time-dependent Schrödinger-type equation (treating propagation distance z in our waveguide system as time):

$$i \frac{\partial}{\partial z} |\psi(z)\rangle = H(z) |\psi(z)\rangle, \quad (2)$$

where $a_n^\dagger(a_n)$ is the creation (annihilation) operator, θ is an initial phase, $A = 2\pi n'_{\text{eff}}/\lambda$ is the modulation amplitude with detuning n'_{eff} , and $\kappa_{n,n+1}$ is the coupling coefficient between the n th and $(n+1)$ th waveguides.

For an initial state $|\psi(0)\rangle$, the light evolution can be expressed as $|\psi(z)\rangle = U(z, 0)|\psi(0)\rangle$, where $U(z, 0) = \mathcal{T} \exp[-i \int_0^z H(z') dz']$ is the unitary evolution operator and \mathcal{T} is the z -ordering operator. According to Floquet theory [32–34], the periodically driven system can be described by quasienergy ε derived from the z -dependent Hamiltonian in Eq. (1) [see Appendix A]. We find that, when the modulation phase difference of neighboring waveguides is inverted ($\varphi = \pi$), special quasienergy collapse [35–37] can occur, which, in turn, creates localization. Below we consider this situation, i.e., out-of-phase modulation on the LNOI waveguide array with waveguide-mode-index engineering, as illustrated in Figs. 1(a) and 1(b), where the width (w) of the waveguide varies along light-propagation direction z with frequency $\Omega = 2\pi/p$ [other cases with

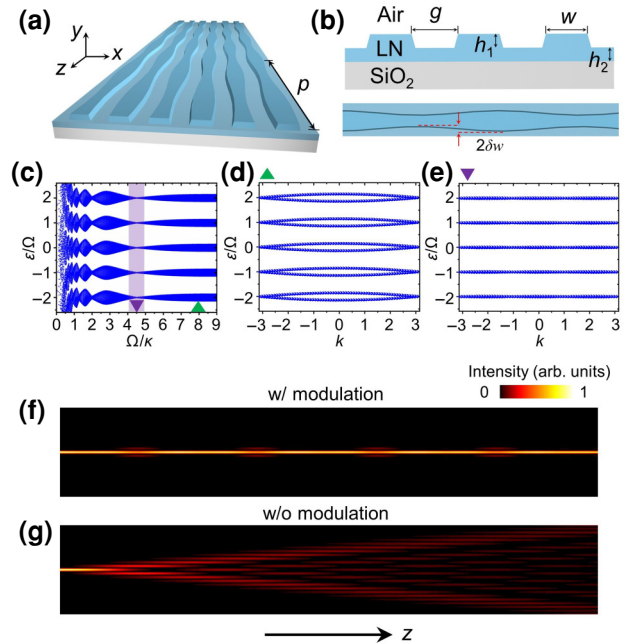


FIG. 1. (a) Schematics of periodically modulated LN waveguides. (b) Cross-section and top view of the waveguides, where $w = 900$ nm, $g = 1000$ nm, $h_1 = h_2 = 300$ nm, and $\delta w = 105$ nm. (c) Floquet-quasienergy spectrum as a function of modulation frequency. Quasienergy collapses around the resonant frequency (purple region). Quasienergy spectrum in the first Brillouin zone with modulation frequency $\Omega = 8\kappa$ (d) and $\Omega = 4.5\kappa$ (e), marked by the upright green triangle and inverted purple triangle, respectively, in (c). Corresponding light-evolution behavior in modulated (f) and normal (g) waveguides. $N = 25$, $A = 5\kappa$, $L = 2L_c$, $L_c = \pi/\kappa$.

arbitrary phase difference φ are demonstrated in Appendix B], and Eq. (1) can be reduced to

$$H(z) = \sum_{n=1}^N \beta_0 a_n^\dagger a_n + \sum_{n=1}^N (-1)^n A \cos(\Omega z + \theta) a_n^\dagger a_n + \sum_{n=1}^{N-1} \kappa_{n,n+1} a_n^\dagger a_{n+1} + h.c. \quad (3)$$

Coupling can be taken as independent of z ($\kappa_{n,n+1} = \kappa_{n+1,n}^* = \kappa$) given that the modulation is weak here ($A \ll \beta_0$) and the spacing between the core of adjacent waveguides remains constant along the propagation direction. By solving Eq. (3), as illustrated in Figs. 1(c)–1(e), Floquet-mode-index modulation at a specific frequency (i.e., resonant frequency) leads to quasienergy band collapse [the pale-purple region in Fig. 1(c)] and flat dispersion in k space [Fig. 1(e)], which are more intriguing than other nonresonant regions [normal dispersion shown in Fig. 1(d)]. For a clearer comparison, Figs. 1(f) and 1(g) show light evolution in the modulated and normal (i.e., without modulation) waveguide array, respectively. Light

remains localized in the input waveguide for the modulated case [Fig. 1(f)] due to quasienergy collapse, suggesting zero crosstalk between neighboring waveguides. In contrast, if one removes modulation, light will couple with other waveguides and exhibit a discrete diffraction phenomenon [Fig. 1(g)].

By applying the substitution $z' = z + \theta/\Omega$ and a unitary transformation in Eq. (3), in the rotating frame we obtain

$$i \frac{\partial}{\partial z'} |\phi(z')\rangle = H'(z') |\phi(z')\rangle, \quad (4)$$

where

$$H' = R^{-1} \left(H - i \frac{\partial}{\partial z'} \right) R, \quad |\psi\rangle = R|\phi\rangle,$$

and

$$R = \sum_{n=1}^N e^{i(-1)^{n+1} \int_0^{z'} A \cos(\Omega z'') dz''} a_n^\dagger a_n$$

is the unitary transformation matrix, which adjusts the phase of the state and the light intensity remains unchanged. So, the coupling between adjacent waveguides is

$$\kappa'_{n,n+1} = \langle \phi'_{n-1} | H' | \phi'_n \rangle = \kappa e^{i(-1)^n \xi \sin(\Omega z')}, \quad (5)$$

where $|\phi'_n\rangle$ is the transverse-waveguide-mode function for the n th waveguide and $\xi = 2A/\Omega = 4\pi n'_{\text{eff}}/(\lambda\Omega)$. Obviously, effective mode-index modulation leads to z -dependent coupling in Eq. (5). Using the Bessel-generating function $\exp[i\xi \sin(\Omega z')] = J_0(\xi) + \sum_{n \neq 0} i^n J_n(\xi) \exp[in\Omega z']$, and neglecting all high-order terms, one gets the effective coupling:

$$\kappa_{\text{eff}} = \kappa J_0(\xi), \quad (6)$$

which is dominated by the zero-order Bessel function, $J_0(\xi)$. It becomes zero when the parameter ξ takes the roots of the function ($\xi_0 \approx 2.405, 5.520\dots$), suggesting the possibility of zero crosstalk in dense integrations.

Notably, Eq. (6) is similar to the result obtained by bending waveguides (the so-called artificial-gauge field [17,31, 38]). Differently, the coupling phase obtained by gauge transformation consists of the dot product of the gauge field and a position vector for bending waveguides [17], which is different from this approach by modulating the effective mode index (the detuning) that can be well interpreted by Floquet engineering. Fortunately, here, the coupling modulation is achieved without having to bend the waveguides, and thus, will not introduce excessive bending losses, which would benefit a low-refractive waveguide system, such as the LNOI waveguide. According to our

experimental results, the propagation losses for mode-index engineering ($\delta w = 0.105 \mu\text{m}$) and artificial-gauge-bending ($A' = 2 \mu\text{m}$) waveguides are 0.57 and 5.81 dB/mm, respectively (see details in Appendix C). Therefore, our scheme would favor large-scale photonic integration.

Notably, although there have been many proposals for light propagation with low crosstalk, they usually work only for a particular wavelength or structure parameter, and broadband crosstalk reduction is still quite challenging. Interestingly, the Floquet modulation here provides flexibility in engineering the dispersion of coupling, which can produce a flat zero-coupling band, and thus, gives rise to broadband and robust zero coupling for densely arranged waveguides (see Appendix D for a theoretical analysis). Therefore, our design demonstrates low-crosstalk transmissions, even if the wavelength or structural parameters vary, as shown in Sec. III.

III. SIMULATIONS AND EXPERIMENTS

The designed shallow-etched-ridge lithium niobate waveguides are 900 nm wide (w) and 300 nm thick (h_1) [see Fig. 1(b)], allowing a fundamental mode (TE) in the broad wavelength region of 1300–2100 nm. The modulation amplitude, period, and initial phase are chosen as $\delta w = 105 \text{ nm}$, $p = 70 \mu\text{m}$, and $\theta = \pi/2$, respectively, to satisfy the resonant (zero-coupling) condition. A commercial finite-element-analysis solver (COMSOL Multiphysics) is employed for full-wave simulations. The simulated effective coupling coefficient between two LN waveguides is shown in Fig. 2(b) (red curve), which matches well with the theoretical prediction (black curve). It is found that, as the modulation amplitude, δw , increases, the effective coupling gradually decreases and becomes negative. There is a critical zero-coupling point ($\kappa_{\text{eff}} = 0$) for a certain modulation strength ($\delta w = 105 \text{ nm}$).

Moreover, we examine the wavelength dependence of the effective coupling. Figure 2(c) shows the theoretical and simulated effective coupling as a function of wavelength (1300–2100 nm) with different modulation amplitudes. The coupling curves become flatter as the modulation increases, implying the reduction of coupling dispersion. As expected, there is a wide wavelength range (around 1400–1700 nm) over which zero coupling and dispersionless coupling are very close, which indicates broadband zero crosstalk [Fig. 2(d)]. For a clearer comparison, optical field evolutions in two coupled waveguides with ($\delta w = 105 \text{ nm}$) and without ($\delta w = 0 \text{ nm}$) modulation are shown in Fig. 2(e). Light remains localized at the input waveguide for the modulation case, even if λ changes. In contrast, light transfers to another waveguide, and the coupling length changes drastically in the conventional one, due to strong dispersion. Figure 2(f) shows the transmissions of two waveguides for the modulation case (solid curve) and conventional

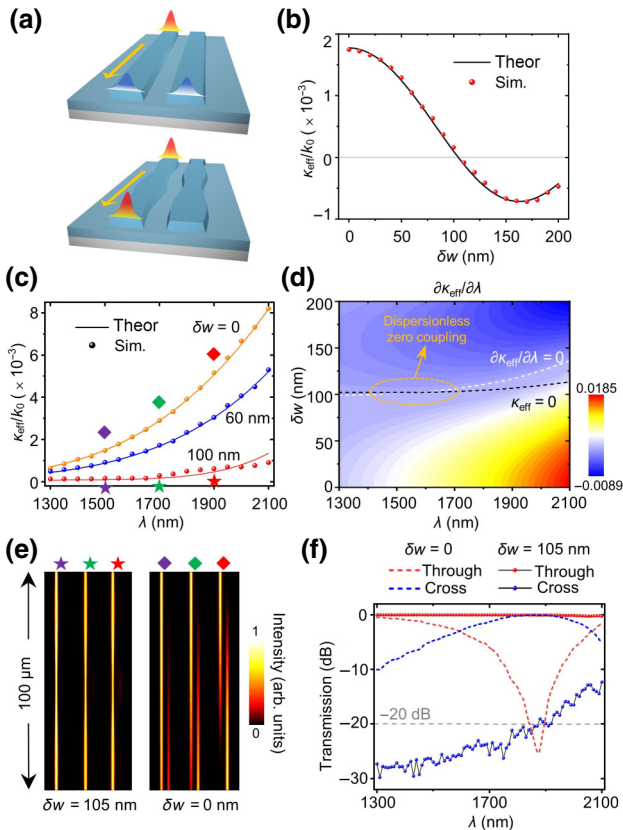


FIG. 2. (a) Schematics of conventional (top) and modulated (bottom) coupled LN waveguides. (b) Effective coupling coefficients as a function of modulation amplitude, δw . Here, $\lambda = 1550$ nm. (c) Effective coupling coefficients as a function of λ . From top to bottom, $\delta w = 0$, 60, and 100 nm. (d) Coupling dispersion $\partial \kappa_{\text{eff}} / \partial \lambda$ as functions of λ and δw ; white dashed curve represents dispersionless coupling ($\partial \kappa_{\text{eff}} / \partial \lambda = 0$) and black dashed curve represents zero coupling ($\kappa_{\text{eff}} = 0$). (e) Simulated optical field dynamics in two coupled waveguides with (left) and without (right) modulation for different wavelengths. (f) Transmissions of coupled waveguides. Solid curves indicate the modulated case and dashed curves for the unmodulated case.

case (dashed curve). The modulated waveguides exhibit high through transmission across a very broad bandwidth (1300–2100 nm), and the crosstalk remains <-20 dB in the spectrum at 1300–1900 nm (bandwidth >600 nm). Although crosstalk increases as the wavelength increases, it is still <-12.5 dB, even for $\lambda = 2100$ nm. In contrast, conventional unmodulated waveguides with the same waveguide pitch show large crosstalk, where the transmission curves exhibit oscillation features as the wavelength varies [dashed curves in Fig. 2(f)].

In experiments, we fabricated modulated LNOI waveguides and normal waveguide samples for comparison (see Appendix E for the fabrication procedure). As shown in Fig. 3(a), the two waveguides are extended to connect with the grating couplers for light input (port I_1 and I_2) and output (port O_1 and O_2). The bottom panels of Fig. 3(a) show

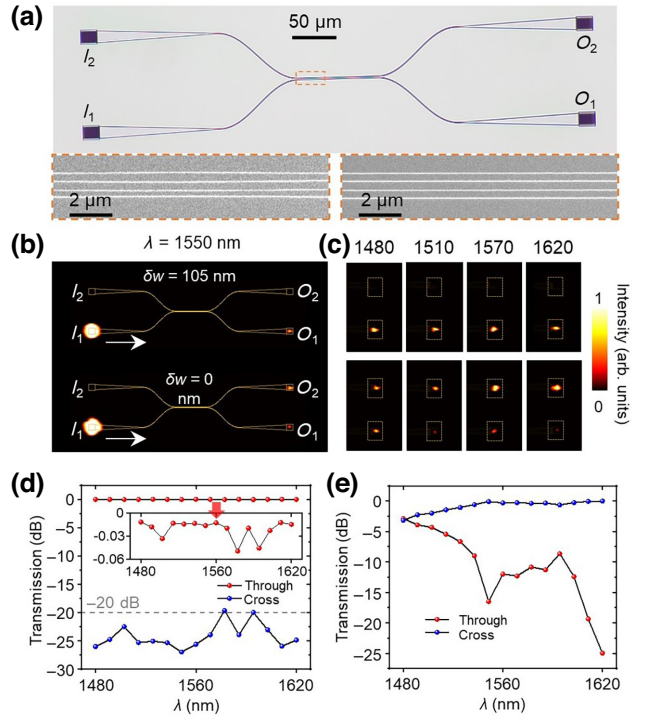


FIG. 3. (a) Top, microscope image of experimental samples on the LNOI platform. Bottom, enlarged scanning-electron-microscopy images of modulated (left) and unmodulated (right) samples. (b) Experimentally recorded light intensities in modulated (top) and conventional (bottom) samples. (c) Intensities of two output ports in modulated (top) and conventional (bottom) samples for different wavelengths (1480, 1510, 1570, and 1620 nm). Experimentally measured transmissions as a function of wavelength for modulated (d) and unmodulated (e) samples.

enlarged pictures of the two samples, where the waveguide width variation can be clearly observed for the modulated samples. A near-infrared laser (1480–1620 nm) is inputted to port I_1 for the two kinds of samples and light-coupling-in and -out signals can be collected by a near-infrared camera (Xeva-1.7-320) through a microscope objective. Figure 3(b) displays the experimentally captured optical propagations for the modulated and normal samples at 1550 nm. Detailed output intensities of different wavelengths (1480, 1510, 1570, and 1620 nm) for the two kinds of samples are displayed in Fig. 3(c). Light obviously couples to neighboring waveguides for the normal samples and the output intensities are influenced by the input wavelength, while it is suppressed in the modulated case for different wavelengths. Measured transmission data of ports O_1 and O_2 for the modulated samples are shown in Fig. 3(d). Crosstalk can be lower than -20 dB across a broad wavelength range from 1480 to 1620 nm. As a comparison, the majority of light energy tends to transfer to the other waveguide across the measured waveband, exhibiting significant crosstalk in this dense arrangement [Fig. 3(e)]. Moreover, we also fabricated samples with intentionally introduced

discrepancies in the waveguide width (± 100 nm deviations), which demonstrated low crosstalk (<−20 dB) in the discrepancy region −40–20 nm (fabrication tolerance, 60 nm) in the experiment, showing good robustness of our scheme (see Appendix D for experimental details).

IV. BROADBAND EIGHT-CHANNEL TRANSMISSION

To further validate the feasibility of our proposal, eight-channel transmission in a dense LN waveguide array is demonstrated with an arbitrary coding input, “10011010,” as shown in Fig. 4(a), here “1” (“0”) represents with (without) light input. The experimentally measured output images of modulated and conventional waveguide arrays with different wavelengths (1530, 1550, and 1570 nm) are shown in Figs. 4(b) and 4(c), respectively [see more experimental results in Appendix F]. The conventional unmodulated case exhibits obvious crosstalk between

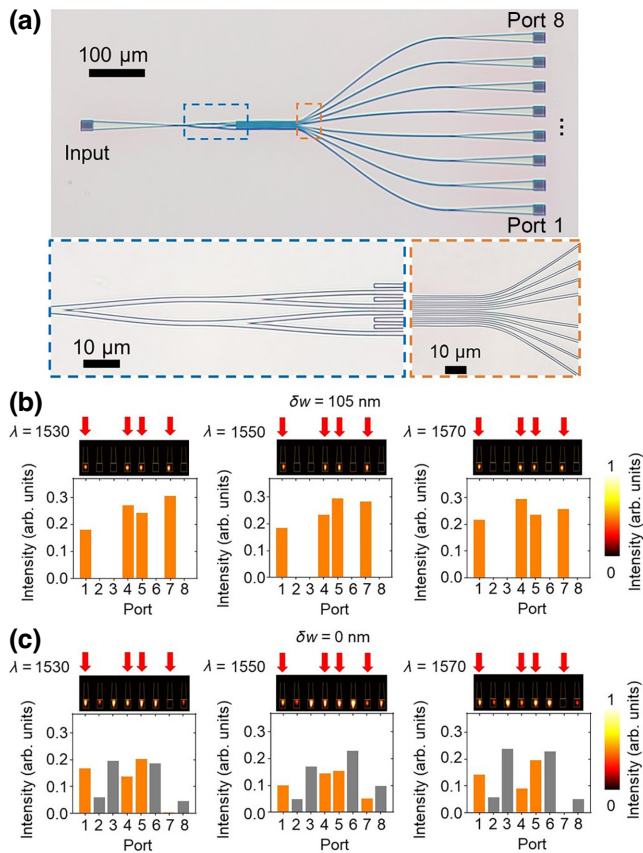


FIG. 4. (a) Microscope image of experimental samples with two enlarged regions showing input (top right) and output (bottom right) channels. Experimentally recorded output intensities (top) and corresponding normalized intensity profiles (bottom) for different wavelengths (1530, 1550, and 1570 nm) in modulated (b) and conventional (c) waveguide arrays. Orange bars indicate light output from the desired channel, while gray bars indicate crosstalk.

waveguides and a lot of energy couples to undesired channels [gray bars in Fig. 4(c)]. However, the optical field can be transmitted with high efficiency in the modulated waveguide array with the same waveguide pitch for different wavelengths [Fig. 4(b)], implying broadband and low-crosstalk multichannel transmission in dense integrations.

V. CONCLUSION AND DISCUSSION

We developed a strategy to realize ultrabroadband low-crosstalk transmission in dense lithium niobate waveguides by Floquet engineering. The underlying physics is attributed to collapse of the quasienergy band by mode-index modulation, which gives rise to broadband zero-coupling effects. We theoretically demonstrate ultrabroadband crosstalk reduction in the wavelength range of 1300–2100 nm, which is further confirmed by experiments, showing <−20-dB crosstalk in the communication band from 1480 to 1620 nm. To validate the feasibility of our scheme, we further demonstrate broadband eight-channel transmission in a compact waveguide network, indicating the potential for large-scale integration.

Different from previous strategies that either utilize the detuning of guided modes to make a mismatch [9,10,15] or suppressing the evanescent field to reduce coupling [13,14,16], here we propose dynamic modulation (i.e., Floquet engineering) to generate a quasiflat band, which can prohibit light diffraction and coupling among waveguides. In principle, this is due to phase modulation in the coupling coefficient [see Eq. (5)], which leads to a cancellation of the total coupling in one propagation period. It is similar to wavy waveguides [20], but without bending loss. Here, we achieve low crosstalk in the LNOI platform. The Floquet-mode-index modulation scheme proposed here is suitable for the LN waveguide because it does not require the fabrication of tiny structures or bending the waveguide, as required by previous strategies, thus enabling waveguide transmissions with lower excess loss compared to the gauge-bending structure. Besides, the reported bandwidth is also very broad (>140 nm for crosstalk <−20 dB, see Table I in Appendix G), thanks to lower material dispersion of the LN materials. Moreover, our strategy also shows good robustness against fabrication errors (<−20 dB, with fabrication tolerance of 110 nm in the simulation and 60 nm in experiments), thus allowing scaling to large circuits. In combination with the electro-optical effects of LN, our approach is expected to be able to control the phase of light in each waveguide in a dense array, thus realizing the optical-field-sweep function, i.e., optical phased array. Other advanced dense and broadband photonic devices, such as chip-scale optical interconnects and space-division multiplexing optical interconnects, are also possible application scenarios for the promising LNOI platform.

ACKNOWLEDGMENTS

The authors acknowledge financial support from the National Key R&D Program of China (Grant No. 2022YFA1404301), the National Natural Science Foundation of China (Grants No. 12174186, No. 12204233, No. 62288101, No. 92250304, and No. 62325504). T.L. is grateful for support from Dengfeng Project B of Nanjing University.

APPENDIX A: FLOQUET THEORY

Equation (1) in the main text is a periodic Hamiltonian, i.e., $H(z) = H(z + p)$, with period $p = 2\pi/\Omega$. A solution of the Schrödinger equation, Eq. (2) in the main text, can be written as a superposition of Floquet states in terms of Floquet theory [32–34]:

$$|\psi_\alpha(z)\rangle = \exp(-i\varepsilon_\alpha z)|u_\alpha(z)\rangle, \quad (\text{A1})$$

where ε_α is the z -independent quasienergy and $|u_\alpha(z)\rangle$ is the associated Floquet mode. By substituting Eq. (A1) into the Schrödinger equation, Eq. (2) in the main text, an eigenvalue equation for ε_α reads

$$\left(H(z) - i\frac{\partial}{\partial z}\right)|u_\alpha(z)\rangle = \varepsilon_\alpha|u_\alpha(z)\rangle. \quad (\text{A2})$$

It should be mentioned that the quasienergies are defined up to integer multiples of ω and the Floquet modes are p -periodic functions, i.e., $|u_\alpha(z + p)\rangle = |u_\alpha(z)\rangle$. To obtain the z -independent Floquet equation, the spectral decompo-

sition method is performed on the Hamiltonian and Floquet modes:

$$H(z) = \sum_{n=-\infty}^{+\infty} e^{-in\Omega z} H_n, \quad (\text{A3})$$

$$|u_\alpha(z)\rangle = \sum_{n=-\infty}^{+\infty} e^{-in\Omega z} |u_\alpha^n\rangle, \quad (\text{A4})$$

and we get

$$(H_0 - n\Omega)|u_\alpha^n\rangle + \sum_{m \neq 0} H_m |u_\alpha^{n-m}\rangle = \varepsilon_\alpha |u_\alpha^n\rangle, (\forall n \in Z). \quad (\text{A5})$$

Now the quasienergy can be calculated in terms of Eq. (A5). First, we rewrite Hamiltonian Eq. (1) as a sum of time-independent and time-periodic parts:

$$H(z) = H_0 + H_p(z), \quad (\text{A6})$$

where

$$H_0 = \sum_{n=1}^N \beta_0 a_n^\dagger a_n + \sum_{n=1}^{N-1} \kappa_{n,n+1} a_n^\dagger a_{n+1} + \text{h.c.}, \quad (\text{A7})$$

$$H_p(z) = \sum_{n=1}^N (-1)^n A \cos(\Omega z + \theta) a_n^\dagger a_n. \quad (\text{A8})$$

Then, we take $\beta_0 = 0$ and express H_0 and H_p as $N \times N$ matrices:

$$H_0 = \begin{pmatrix} 0 & \kappa & 0 & \cdots \\ \kappa & 0 & \kappa & \\ 0 & \kappa & 0 & \\ \vdots & & & \ddots \end{pmatrix}_{N \times N}, \quad (\text{A9})$$

$$H_p(z) = \frac{A}{2} \begin{pmatrix} e^{i\theta} e^{i\Omega z} e^{i\varphi} + e^{-i\theta} e^{-i\Omega z} e^{-i\varphi} & 0 & \cdots \\ 0 & e^{i\theta} e^{i\Omega z} + e^{-i\theta} e^{-i\Omega z} & 0 \\ \vdots & 0 & e^{i\theta} e^{i\Omega z} e^{i\varphi} + e^{-i\theta} e^{-i\Omega z} e^{-i\varphi} \\ & & \ddots \end{pmatrix}_{N \times N}, \quad (\text{A10})$$

$$= H_1 e^{i\Omega z} + H_{-1} e^{-i\Omega z},$$

where

$$H_{\pm 1} = \frac{A}{2} \begin{pmatrix} e^{\pm i\theta} e^{\pm i\varphi} & & \\ & e^{\pm i\theta} & \\ & e^{\pm i\theta} e^{\pm i\varphi} & \cdots \\ & & \ddots \end{pmatrix}_{N \times N}. \quad (\text{A11})$$

So, time-independent Eq. (A5) can be represented as the following eigenvalue problem with a block-matrix operator:

$$\begin{pmatrix} \ddots & & & \\ & H_0 + \Omega & H_{-1} & \\ & H_{+1} & H_0 & H_{-1} \\ & & H_{+1} & H_0 - \Omega \end{pmatrix} \begin{pmatrix} \vdots \\ u_\alpha^{-1} \\ u_\alpha^0 \\ u_\alpha^{+1} \\ \vdots \end{pmatrix} = \varepsilon_\alpha \begin{pmatrix} \vdots \\ u_\alpha^{-1} \\ u_\alpha^0 \\ u_\alpha^{+1} \\ \vdots \end{pmatrix}, \quad (\text{A12})$$

then the quasienergy can be calculated and is demonstrated in Fig. 1 in the main text.

APPENDIX B: EFFECTS OF MODULATION PHASE

Here, we analyze how the modulation phase difference of adjacent waveguides affects the evolution of light. We have calculated the quasienergy bands for different phase differences ($\varphi = 3\pi/4, \pi/2, \pi/4, 0$), as shown in

Figs. 5(a)–5(d). When φ deviates slightly from π , such as $\varphi = 3\pi/4$ in Fig. 5(a), the quasienergy-band collapse still exists and the corresponding light evolution retains well-localized behavior [Fig. 5(e)]. As φ continues to decrease, the modulation frequency of the quasienergy-band-collapse region [purple inverted triangles in Figs. 5(a)–5(d)] decreases and the collapsed region interacts with other quasienergy bands, resulting in a weak collapse effect, while the light field no longer remains well localized [Figs. 5(f)–5(h)]. For $\varphi = 0$, which is

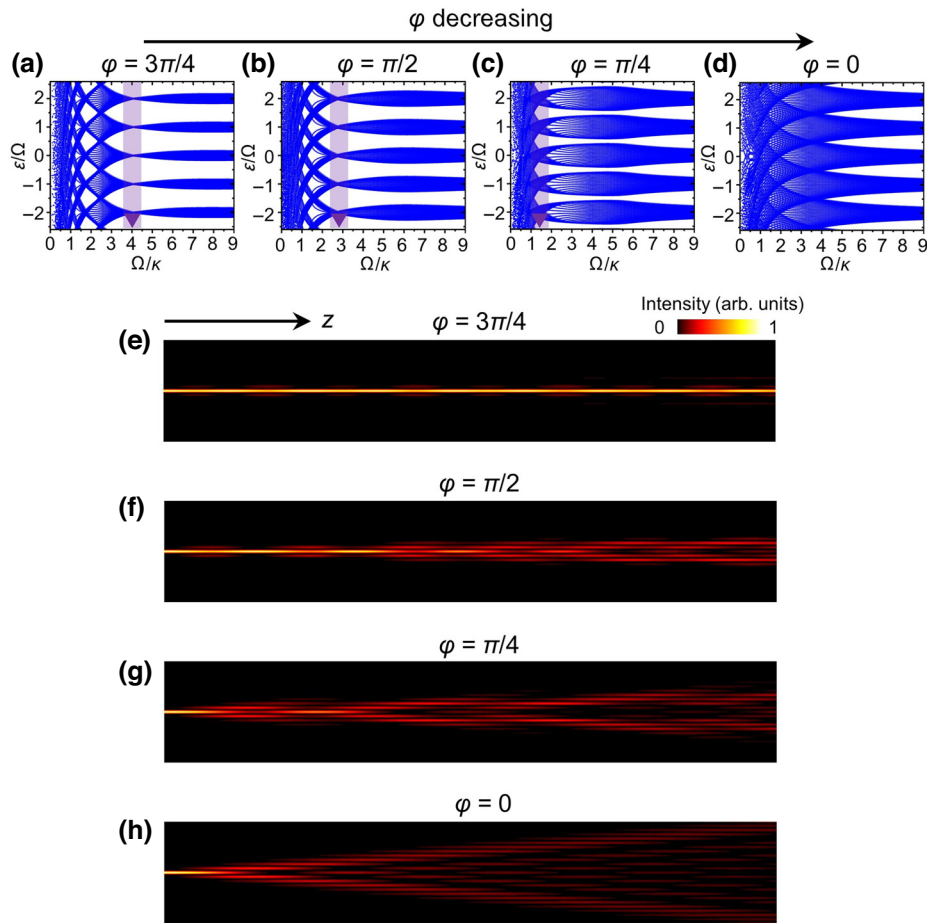


FIG. 5. (a)–(d) Floquet-quasienergy spectrum as a function of modulation frequency with different modulation phase differences, φ . Quasienergy-band-collapse regions move in the direction of decreasing frequency, Ω , when φ decreases to 0. (e)–(h) Corresponding light-evolution behavior. All parameters are consistent with Fig. 1, except for φ and Ω : $\Omega = 4.05\kappa$ (e), 2.8κ (f), 1.5κ (g), and 3.5κ (h).

equivalent to in-phase modulation, light always exhibits the same diffraction behavior, regardless of the modulation frequency. It is for these reasons that we have mainly studied the case of $\varphi = \pi$ in the main text, as it exhibits the best localization effect.

APPENDIX C: LOSS MEASUREMENTS

It is found that zero coupling can be realized for artificial-gauge-bending waveguides with bending amplitude $A' = 2 \mu\text{m}$ and modulation period $p = 70 \mu\text{m}$ [see Fig. 6(b)]. However, light obviously leaks into the cladding and indicates excess loss. We carried out experiments to measure the propagation losses of Floquet-mode-index engineering ($\delta w = 0.105 \mu\text{m}$) and artificial-gauge-bending ($A' = 2 \mu\text{m}$) waveguides (a straight waveguide is also measured for comparison), as shown in Fig. 6. We fabricate single waveguides with different lengths for each set, as shown in Fig. 6(a). In the experiment, the laser is incident on the input grating (the input power is denoted by P_{in} ; here, $P_{\text{in}} = 10 \text{ mW}$) through a single-mode fiber, then the transmission signals are collected by another fiber and

connected to an optical power meter to measure the output intensity (P_{out}). The results are shown in Fig. 6(c) with the fitting curve, where the slope represents the propagation loss, α . It is shown that the losses for a straight waveguide, Floquet-mode-index-engineering waveguide, and artificial-gauge-bending waveguide are about 0.53, 0.57, and 5.81 dB/mm, respectively. These results illustrate that the losses in Floquet-mode-index engineering and straight waveguides are very close to each other, while the bending waveguide has significant propagation loss, which demonstrates lower-loss superiority compared to the bending scheme, and it is more applicable for low-crosstalk large-scale photonic integration. Additionally, we also obtain loss data for the grating coupler, which is found to be about 11–12 dB by fitting the intercepts of the curves.

APPENDIX D: BROADBAND AND ROBUSTNESS ANALYSIS

Here, we focus on the dispersion of coupling and crosstalk reduction. To highlight the wavelength dependence of coupling, we rewrite the expression as $\kappa_{\text{eff}}(\lambda)$ and calculate the derivative of κ_{eff} to λ , so the coupling

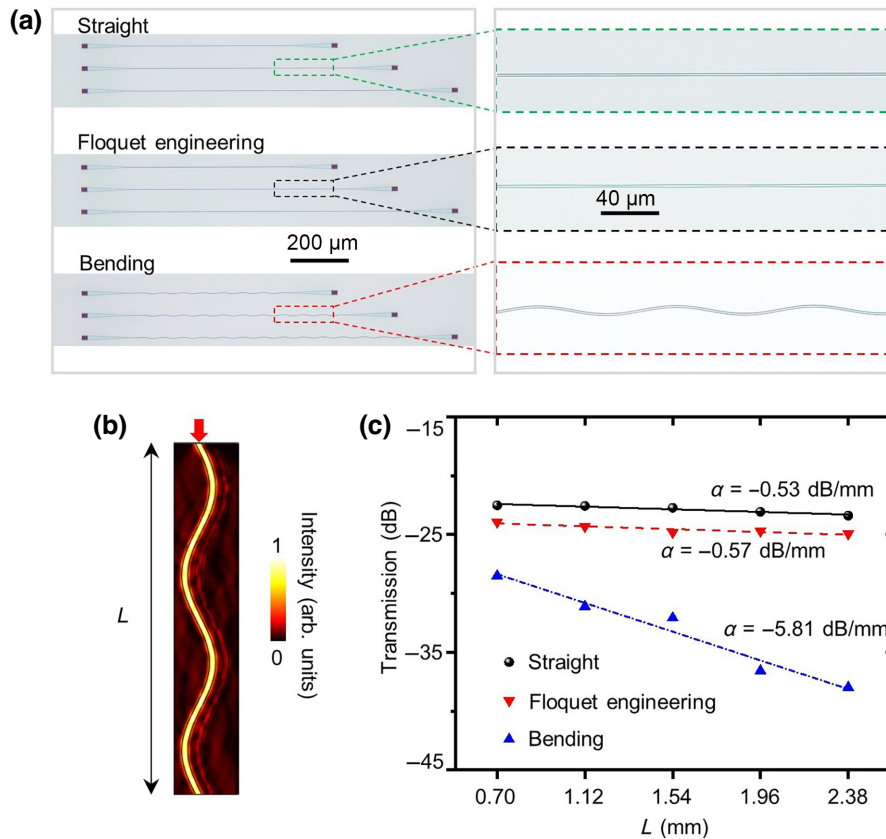


FIG. 6. (a) Microscope image of single-waveguide samples with different lengths. From top to bottom, straight, mode-index Floquet engineering, and bending waveguides. Magnifications of the structures are shown in the right panel. (b) Simulation results for crosstalk reduction in dual artificial-gauge-bending LNOI waveguides. $w = 900 \text{ nm}$, $h = 300 \text{ nm}$, $g = 1000 \text{ nm}$, $L = 140 \mu\text{m}$, $\theta = \pi/2$, $A' = 2 \mu\text{m}$, and $p = 70 \mu\text{m}$. (c) Experimental results of propagation loss for different waveguide configurations.

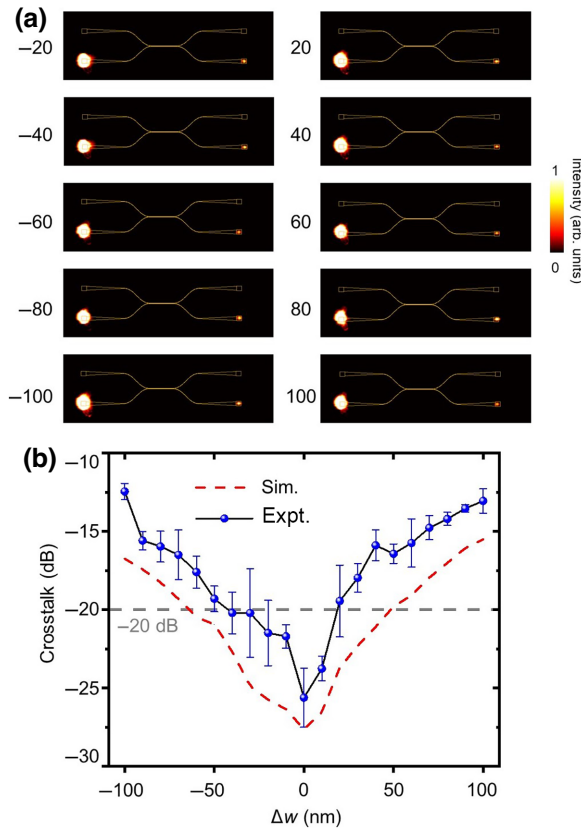


FIG. 7. (a) Experimental output of LNOI samples with intentionally introduced fabrication errors. (b) Simulation and experimental crosstalk for different fabrication errors, Δw . Central wavelength in our design is $\lambda = 1550$ nm.

dispersion is written as

$$\frac{\partial \kappa_{\text{eff}}(\lambda)}{\partial \lambda} = J_0(\xi) \frac{\partial \kappa}{\partial \lambda} + \kappa J_1(\xi) \frac{\partial \xi}{\partial \lambda}. \quad (\text{D1})$$

It is intuitive that the effective coupling dispersion is determined by the first term, the coupling dispersion, and the second one, the modulation-induced dispersion. Around zero effective coupling, i.e., $J_0(\xi_0) \approx 0$, the intrinsic coupling dispersion is fully suppressed, so the wavelength dependence of crosstalk reduction is just determined by the modulation-induced dispersion. Notably, ξ is a function of detuning, n'_{eff} , which indicates that modulation-induced dispersion is related to the material dispersion. Because the LNOI we use here has lower material dispersion

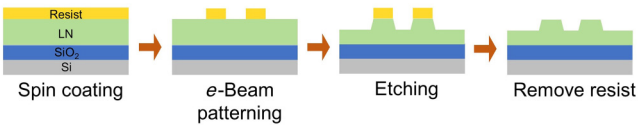


FIG. 8. Fabrication process for the lithium niobate waveguides.

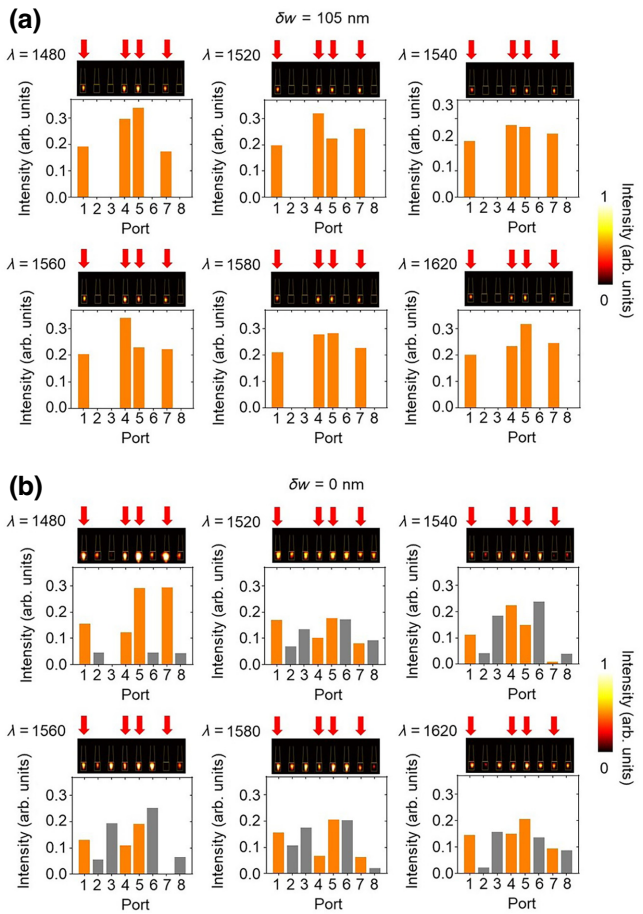


FIG. 9. Eight-channel light transmissions (10011010) at different wavelengths in modulated (a) and normal (b) eight-channel waveguide arrays.

(compared to SOI), it is promising for achieving broadband crosstalk reduction.

We have demonstrated theoretically and experimentally in the main text the ultrabroadband feature of our scheme. To further clarify the mechanism of robustness, we keep the pitch constant and purposely change the width ($w + \Delta w$) and spacing ($g - \Delta w$) of the waveguides with fabrication error Δw , which is commonly encountered in practical fabrication processes. Similar to the dispersion analysis in Eq. (D1), we calculate the derivative of κ_{eff} to Δw and obtain

$$\frac{\partial \kappa_{\text{eff}}}{\partial \Delta w} = J_0(\xi) \frac{\partial \kappa}{\partial \Delta w} + \kappa J_1(\xi) \frac{\partial \xi}{\partial \Delta w} \approx J_0(\xi) \frac{\partial \kappa}{\partial \Delta w}. \quad (\text{D2})$$

Notably, $\xi = 4\pi n'_{\text{eff}}/(\lambda\omega)$ and the detuning, n'_{eff} , are mainly determined by δw and almost negligibly influenced by Δw , so we can neglect the term $\partial \xi / \partial \Delta w \approx 0$ and get the approximation in Eq. (D2). Since we are only concerned with the vicinity of the resonance region

TABLE I. Comparison of crosstalk-reduction schemes in an integrated photonics platform.

| Ref. | Platform | Structure | Bandwidth ^a (nm) | Structural tolerance (nm) | Crosstalk (dB) | Pitch (nm) |
|-----------|----------|---------------------|-----------------------------|---------------------------|----------------|-------------------|
| This work | L NOI | Floquet engineering | >600 theor >140 expt. | 110 theor 60 expt. | <-20 | 1900 ^b |
| [9] | SOI | Superlattice | >70 | ... | <-20 | 780 |
| [15] | | | 100 | ... | <-20 | 800 |
| [10] | | | 80 | ... | <-19.5 | 780 |
| [13] | | Extreme-skin-depth | ... | ... | <-30 | 1000 |
| [14] | | waveguides | >80 | ... | -30 to -60 | 870–1000 |
| [16] | | Artificial gauge | ~80 | ... | -50 | 1190 |
| [17] | | bending | ~50 | ... | <-20 | 770 |
| [18] | | | >20 | 40 | -26 | 695 |
| [19] | | | >40 | ... | -18 | 695 |
| [20] | | | 120 | ... | -30 | 750 |
| [11] | | Inverse design | >60 | ... | -22.9 | 600 |

^aHere, bandwidth is defined as the range of wavelength where crosstalk <-20 dB; some studies actually have a wider bandwidth but are not fully demonstrated, so we denote them by “>.”

^bThe pitch of L NOI waveguides is larger than that of SOI waveguides due to their low refractive index.

($\xi \approx \xi_0, J_0(\xi) \approx 0$), the effective coupling is tolerant of the fabrication errors ($\partial \kappa_{\text{eff}} / \partial \Delta w \approx 0$).

To confirm the theoretical results, we designed 20 samples that intentionally introduced fabrication errors ($\Delta w = \pm 10, \pm 20, \dots, \pm 100$ nm). As illustrated in Fig. 7(a), the experimental results show that light remains in the excited channel, although fabrication errors are introduced. The simulation and experimental results of crosstalk are demonstrated in Fig. 7(b); crosstalk can remain below -20 dB in error regions -60–50 nm (fabrication tolerance, 110 nm) and -40–20 nm (fabrication tolerance, 60 nm), respectively, which shows good robustness of our scheme.

APPENDIX E: FABRICATION OF LITHIUM NIOBATE WAVEGUIDES

The devices are fabricated based on 600-nm-thick X-cut lithium niobate with 2-μm-thick SiO₂ substrate and air cladding. The experimental samples were fabricated using electron-beam lithography (EBL) and a dry-etching process (see Fig. 8). The substrates were cleaned in an ultrasound bath with acetone, isopropyl alcohol, and deionized water for 15 min each and dried under a flow of clean nitrogen. After that, the waveguide arrays and grating nanostructures were exposed to EBL. The samples were then used to dry etch the lithium niobate layer in a 16:1 mixture of Ar and CHF₃ plasma, and the residual photoresist was stripped off by an oxygen-plasma stripper.

APPENDIX F: ADDITIONAL EXPERIMENTAL RESULTS FOR THE EIGHT-CHANNEL WAVEGUIDE ARRAY

Experimentally measured transmissions of the modulated ($\delta_w = 0.105$ μm) and conventional ($\delta_w = 0$ μm) eight-channel waveguide arrays with different wavelengths

(1480, 1520, 1540, 1560, 1580, and 1620 nm) are shown in Figs. 9(a) and 9(b), respectively. The optical field can be transmitted with high efficiency in the modulated waveguide array, while it exhibits obvious crosstalk between waveguides for conventional unmodulated case.

APPENDIX G: COMPARISON OF CROSSTALK-REDUCTION SCHEMES IN INTEGRATED PHOTONICS PLATFORMS

Table I shows the comparison of crosstalk-reduction schemes in an integrated photonics platform. The reported bandwidth in this work is very broad and shows good robustness against fabrication errors.

- [1] D. A. B. Miller, Device requirements for optical interconnects to silicon chips, *Proc. IEEE* **97**, c1166 (2009).
- [2] Q. Cheng, M. Bahadori, M. Glick, S. Rumley, and K. Bergman, Recent advances in optical technologies for data centers: A review, *Optica* **5**, 1354 (2018).
- [3] D. J. Richardson, J. M. Fini, and L. E. Nelson, Space-division multiplexing in optical fibres, *Nat. Photonics* **7**, 354 (2013).
- [4] B. J. Puttnam, G. Rademacher, and R. S. Luís, Space-division multiplexing for optical fiber communications, *Optica* **8**, 1186 (2021).
- [5] J. Feldmann, N. Youngblood, M. Karpov, H. Gehring, X. Li, M. Stappers, M. Le Gallo, X. Fu, A. Lukashchuk, A. S. Raja, J. Liu, C. D. Wright, A. Sebastian, T. J. Kippenberg, W. H. P. Pernice, and H. Bhaskaran, Parallel convolutional processing using an integrated photonic tensor core, *Nature* **589**, 52 (2021).
- [6] C. M. Wu, H. S. Yu, S. Lee, R. M. Peng, I. Takeuchi, and M. Li, Programmable phase-change metasurfaces on waveguides for multimode photonic convolutional neural network, *Nat. Commun.* **12**, 96 (2021).

- [7] F. Ashtiani, A. J. Geers, and F. Aflatouni, An on-chip photonic deep neural network for image classification, *Nature* **606**, 501 (2022).
- [8] X. D. Fan and I. M. White, Optofluidic microsystems for chemical and biological analysis, *Nat. Photonics* **5**, 591 (2011).
- [9] W. Song, R. Gatdula, S. Abbaslou, M. Lu, A. Stein, W. Y. Lai, J. Provine, R. F. Pease, D. N. Christodoulides, and W. Jiang, High-density waveguide superlattices with low crosstalk, *Nat. Commun.* **6**, 7027 (2015).
- [10] R. Gatdula, S. Abbaslou, M. Lu, A. Stein, and W. Jiang, Guiding light in bent waveguide superlattices with low crosstalk, *Optica* **6**, 585 (2019).
- [11] B. Shen, R. Polson, and R. Menon, Increasing the density of passive photonic-integrated circuits via nanophotonic cloaking, *Nat. Commun.* **7**, 13126 (2016).
- [12] L. H. Gabrielli, D. Liu, S. G. Johnson, and M. Lipson, On-chip transformation optics for multimode waveguide bends, *Nat. Commun.* **3**, 1217 (2012).
- [13] S. Jahani, S. Kim, J. Atkinson, J. C. Wirth, F. Kalhor, A. A. Norman, W. D. Newman, P. Shekhar, K. Han, V. Van, R. G. DeCorby, L. Chrostowski, M. Qi, and Z. Jacob, Controlling evanescent waves using silicon photonic all-dielectric metamaterials for dense integration, *Nat. Commun.* **9**, 1893 (2018).
- [14] M. B. Mia, S. Z. Ahmed, I. Ahmed, Y. J. Lee, M. Qi, and S. Kim, Exceptional coupling in photonic anisotropic metamaterials for extremely low waveguide crosstalk, *Optica* **7**, 881 (2020).
- [15] L.-M. Leng, Y. Shao, P.-Y. Zhao, G.-F. Tao, S.-N. Zhu, and W. Jiang, Waveguide superlattice-based optical phased array, *Phys. Rev. Appl.* **15**, 014019 (2021).
- [16] M. F. Kabir, M. B. Mia, I. Ahmed, N. Jaidye, S. Z. Ahmed, and S. Kim, Anisotropic leaky-like perturbation with sub-wavelength gratings enables zero crosstalk, *Light: Sci. Appl.* **12**, 135 (2023).
- [17] W. Song, T. Li, S. Wu, Z. Wang, C. Chen, Y. Chen, C. Huang, K. Qiu, S. Zhu, Y. Zou, and T. Li, Dispersionless coupling among optical waveguides by artificial gauge field, *Phys. Rev. Lett.* **129**, 053901 (2022).
- [18] X. Yi, H. Zeng, S. Gao, and C. Qiu, Design of an ultra-compact low-crosstalk sinusoidal silicon waveguide array for optical phased array, *Opt. Express* **28**, 37505 (2020).
- [19] X. Yi, Y. Zhang, H. Zeng, S. Gao, S. Guo, and C. Qiu, Demonstration of an ultra-compact 8-channel sinusoidal silicon waveguide array for optical phased array, *Opt. Lett.* **47**, 226 (2022).
- [20] P. J. Zhou, T. Li, Y. C. Lin, L. P. Xia, L. Shen, X. C. Xu, T. Li, and Y. Zou, Artificial gauge field enabled low-crosstalk, broadband, half-wavelength pitched waveguide arrays, *Laser Photonics Rev.* **17**, 2200944 (2023).
- [21] M. Xu, M. He, H. Zhang, J. Jian, Y. Pan, X. Liu, L. Chen, X. Meng, H. Chen, Z. Li, X. Xiao, S. Yu, S. Yu, and X. Cai, High-performance coherent optical modulators based on thin-film lithium niobate platform, *Nat. Commun.* **11**, 3911 (2020).
- [22] M. B. He, M. Y. Xu, Y. X. Ren, J. Jian, Z. L. Ruan, Y. S. Xu, S. Q. Gao, S. H. Sun, X. Q. Wen, L. D. Zhou, L. Liu, C. J. Guo, H. Chen, S. Y. Yu, L. Liu, and X. L. Cai, High-performance hybrid silicon and lithium niobate Mach-Zehnder modulators for 100 Gbit s⁻¹ and beyond, *Nat. Photonics* **13**, 359 (2019).
- [23] B. Desiatov, A. Shams-Ansari, M. Zhang, C. Wang, and M. Loncar, Ultra-low-loss integrated visible photonics using thin-film lithium niobate, *Optica* **6**, 380 (2019).
- [24] Y. Qi and Y. Li, Integrated lithium niobate photonics, *Nanophotonics* **9**, 1287 (2020).
- [25] C. Wang, M. Zhang, X. Chen, M. Bertrand, A. Shams-Ansari, S. Chandrasekhar, P. Winzer, and M. Loncar, Integrated lithium niobate electro-optic modulators operating at CMOS-compatible voltages, *Nature* **562**, 101 (2018).
- [26] A. Boes, B. Corcoran, L. Chang, J. Bowers, and A. Mitchell, Status and potential of lithium niobate on insulator (LNOI) for photonic integrated circuits, *Laser Photonics Rev.* **12**, 1700256 (2018).
- [27] D. Zhu, L. B. Shao, M. J. Yu, R. Cheng, B. Desiatov, C. J. Xin, Y. W. Hu, J. Holzgrafe, S. Ghosh, A. Shams-Ansari, E. Puma, N. Sinclair, C. Reimer, M. A. Zhang, and M. Loncar, Integrated photonics on thin-film lithium niobate, *Adv. Opt. Photonics* **13**, 242 (2021).
- [28] G. G. Pyrialakos, J. Beck, M. Heinrich, L. J. Maczewsky, N. V. Kantartzis, M. Khajavikhan, A. Szameit, and D. N. Christodoulides, Bimorphic Floquet topological insulators, *Nat. Mater.* **21**, 634 (2022).
- [29] L. J. Maczewsky, J. M. Zeuner, S. Nolte, and A. Szameit, Observation of photonic anomalous Floquet topological insulators, *Nat. Commun.* **8**, 13756 (2017).
- [30] S. Mukherjee, A. Spracklen, M. Valiente, E. Andersson, P. Ohberg, N. Goldman, and R. R. Thomson, Experimental observation of anomalous topological edge modes in a slowly driven photonic lattice, *Nat. Commun.* **8**, 13918 (2017).
- [31] M. C. Rechtsman, J. M. Zeuner, Y. Plotnik, Y. Lumer, D. Podolsky, F. Dreisow, S. Nolte, M. Segev, and A. Szameit, Photonic Floquet topological insulators, *Nature* **496**, 196 (2013).
- [32] M. Bukov, L. D'Alessio, and A. Polkovnikov, Universal high-frequency behavior of periodically driven systems: from dynamical stabilization to Floquet engineering, *Adv. Phys.* **64**, 139 (2015).
- [33] A. Eckardt, Colloquium: Atomic quantum gases in periodically driven optical lattices, *Rev. Mod. Phys.* **89**, 011004 (2017).
- [34] Z. Fedorova Cherpakova, C. Jorg, C. Dauer, F. Letscher, M. Fleischhauer, S. Eggert, S. Linden, and G. von Freymann, Limits of topological protection under local periodic driving, *Light: Sci. Appl.* **8**, 63 (2019).
- [35] K. Staliunas and C. Masoller, Subdiffractive light in bi-periodic arrays of modulated fibers, *Opt. Express* **14**, 10669 (2006).
- [36] I. L. Garanovich, S. Longhi, A. A. Sukhorukov, and Y. S. Kivshar, Light propagation and localization in modulated photonic lattices and waveguides, *Phys. Rep.* **518**, 1 (2012).
- [37] A. Szameit, Y. V. Kartashov, F. Dreisow, M. Heinrich, T. Pertsch, S. Nolte, A. Tunnermann, V. A. Vysloukh, F. Lederer, and L. Torner, Inhibition of light tunneling in waveguide arrays, *Phys. Rev. Lett.* **102**, 153901 (2009).
- [38] Y. Lumer, M. A. Bandres, M. Heinrich, L. J. Maczewsky, H. Herzog-Sheinfux, A. Szameit, and M. Segev, Light guiding by artificial gauge fields, *Nat. Photonics* **13**, 339 (2019).